70th International Astronautical Congress (IAC), Washington D.C., United States, 21-25 October 2019.

IAC-19-C4.5.1

Effect of Ion Thruster Plume-Thermosphere Interaction on Satellite Drag in Very Low Earth Orbit

Shaun M. Andrews[a]*, Lucinda Berthoud[a]

[a] *Department of Aerospace Engineering, Queen's Building, University Walk, Bristol, BS8 1TR, United Kingdom*
* Corresponding Author, sa15339@my.bristol.ac.uk

Abstract

This work presents a study of the interactions of an ion thruster plume within the thermosphere of Very Low Earth Orbit (VLEO), in the context of a drag-compensation mission. VLEO is a highly appealing region for spacecraft operations, as reducing the operational altitude of remote sensing payloads improves radiometric performance and spatial resolution, whilst reducing the size, mass, power requirement and cost of instruments. The analysis is performed with a hybrid Direct Simulation Monte-Carlo/Particle-in-Cell (DSMC-PIC) code and includes a variable hard sphere model to calculate elastic cross sections for *Xe*-thermosphere momentum collisions and analytical approaches to infer Xe^+-thermosphere charge-exchange cross sections. The effect on the satellite coefficient of drag is determined, and it is shown that aerodynamic models of VLEO satellites are incomplete without the inclusion of plume interactions.

Keywords: Ion Thrusters, Orbital Aerodynamics, Direct Simulation Monte-Carlo, Particle-in-Cell, Very Low Earth Orbit, Drag Compensating Electric Propulsion

Nomenclature

$\mathbb{R}_u$	Uniformly Distributed Random Number
A_e	Exhaust Exit Area [m^2]
A_f	Frontal Area [m^2]
C_D	Coefficient of Drag
E_B	Ionisation Potential [eV]
R_∞	Rydberg Constant [/m]
V_b	Beam Voltage [V]
a_0	Bohr Radius [m]
k_B	Boltzmann Constant [eV/K]
$m_{S/C}$	Satellite Mass [kg]
v_e	Exhaust Velocity [m/s]
$\boldsymbol{a_{drag}}$	Drag Acceleration [m/s]
$\boldsymbol{v_{rel}}$	Relative Velocity [m/s]
α_T	Thermal Accommodation Coefficient
η_i	Ionisation Efficiency
λ_D	Debye Length [m]
ρ_C	Macroscopic Charge Density [C/m^3]
ϵ_0	Permittivity of Free Space [s^{4}A^2/kgm^3]
h	Planck's Constant [m^{2}kg/s]
t	Simulation Time [s]
Γ	Gamma Function
ΔE	Energy Defect [eV]
Δt	Time-Step [s]
$\Delta x, \Delta y$	Cell Spacing [m]
P	Collision Probability
Φ	Electric Potential [V]
A	General Thermospheric Species
Ap	Geomagnetic Activity Index
$F10.7$	Solar Radio Flux at 10.7cm [sfu]
Kn	Knudsen Number
M	Mach Number
P	Pressure [Pa]
T	Temperature [K]
f	Spatial Distribution Function
g	Relative Particle Velocity [m/s]
m	Particle Mass [amu]
$n,\ nd$	Macroscopic Number Density [#/m^3]
p	Particle Momentum [kgm/s]
q	Particle Charge [C]
v	Vertical Velocity [m/s]
x	Horizontal Displacement [m]
y	Vertical Displacement [m]
$\boldsymbol{B}$	Magnetic Field [T]
$\boldsymbol{E}$	Electric Field [N/C]
$\boldsymbol{F}$	External Force on f [N]
$\boldsymbol{T}$	Thrust [N]
$\boldsymbol{c}$	Particle Velocity [m/s]
$\boldsymbol{x}$	Particle Position [m]
ν	Electron Viscosity [m^2/s]
ρ	Atmospheric Density [kg/m^3]
σ	Collision Cross-Section [Å^2]
ω	DSMC Viscosity Index

Subscript/Superscript

$'$	Post-Collision
0	Quasi-Neutral Reference Condition
a	Ambient
b	Primary Beam Property
e	Electrons
i	Subset of Ionic (Charged) Species
k	Set of Total Particle Species
n	Subset of Neutral Species
S/C	Spacecraft
w	Thruster Wall

Ave	Average
REF	DSMC Reference Condition

Acronyms/Abbreviations

CEX	Charge-Exchange
DSMC	Direct Simulation Monte-Carlo
ESA	European Space Agency
GOCE	Gravity Field and Steady-State Ocean Circulation Explorer
JAXA	Japan Aerospace Exploration Agency
MCC	Monte-Carlo Collisions
MEX	Momentum-Exchange
NRLMSISE	Naval Research Laboratory Mass Spectrometer and Incoherent Scatter Radar Exosphere
NTC	No-Time-Counter
PIC	Particle-in-Cell
QN	Quasi-Neutral
SLATS	Super Low Altitude Test Satellite
SSO	Sun-Synchronous Orbit
VHS	Variable Hard Sphere
VLEO	Very Low Earth Orbit

1. Introduction

Satellite operations in Very Low Earth Orbit (VLEO), which describes the region of orbital altitudes below 250km, are highly appealing for flexible, high-performing and economical spacecraft operations to deliver low-cost communications and Earth observation data [1]. Ground resolution is directly proportional to altitude; therefore, instrument volume, mass and cost reduces with altitude for the same performance [2,3]. The radiometric resolution also improves according to the inverse-square of altitude, yielding higher signal-to-noise ratios. VLEO can therefore provide substantial improvements in the performance of Earth remote sensing payloads for applications such as meteorology, oceanic circulation, polar ice, wildfires, agriculture, urban mapping or military surveillance. VLEO satellites also benefit from improved communications latency and link budget [4], and the launch vehicles can provide greater payload mass fractions. Concerns over the increasing debris population in commercially exploited orbits is avoided.

However, the mission lifetime in VLEO is significantly limited. Aerodynamic drag, due to the momentum exchange between the upper thermosphere and satellite, reduces the orbital energy. The result is change in eccentricity towards a more circular orbit, and reduction of semi-major axis until the satellite's inevitable re-entry. To maintain altitude in VLEO, a satellite therefore requires regular pro-grade manoeuvres, or a method of continuous low-thrust drag compensation. The high specific impulses of ion thrusters, allows continuous compensation for the variable decelerations experienced by a satellite due to atmospheric drag [5], without the vibrations and limited mission lifetime with the use of conventional chemically powered rocket engines, which are capable only of restoring the path of the host satellite to a purely inertial trajectory.

Recently, drag-compensated operation in VLEO has been exploited as a result of component miniaturisation and cost-reduction, with demand for high resolution data. The European Space Agency's (ESA) Gravity Field and Steady-State Ocean Circulation Explorer (GOCE) was launched in 2009 [6]. GOCE used a QinetiQ T5(UK-10) ion thruster to compensate for the orbital decay, sustaining an orbital altitude of 250-265km for 55 months before expending its fuel. The Super Low Altitude Test Satellite (SLATS) 'Tsubame' was launched in 2017 by the Japan Aerospace Exploration Agency (JAXA), with the objectives to understand the effects of high-density atomic oxygen on the satellite and to verify drag-compensation feasibility with a Kiku-8 ion thruster [7]. It will enter the drag-compensating 180-250km phase of its mission in late 2019.

It was shown by Walsh and Berthoud [8,9] that, regardless of local time at the ascending node or thrust regime, at a nominal altitude of 190km an ion thruster propulsion system would need at least 1.5 times the cruise thrust to ensure it could recover from an altitude of 180km in the worst-case of a malfunction. It was also seen that more thrust was required to maintain a noon sun-synchronous orbit (SSO) than a Dawn-Dusk SSO (between 37% and 62% more from 160km to 250km). Detailed spacecraft drag modelling in VLEO is thus essential if the propulsion assembly is to be designed correctly for the mission lifetime requirement. The propellent required is proportional to the pre-determined mission delta-V, the budget for which is given by the expected mission drag forces. A common approach to calculate the drag acceleration experienced by a blunt-bodied spacecraft is

$$\boldsymbol{a_{drag}} = -\frac{1}{2}\rho\frac{C_D A_f}{m} v_{rel}^2 \frac{\boldsymbol{v_{rel}}}{\|\boldsymbol{v_{rel}}\|} \quad (1)$$

A good estimation of $\boldsymbol{a_{drag}}$ is often difficult to obtain [10]. This is due to the large uncertainties associated with ρ , $\boldsymbol{v_{rel}}$ and C_D. It is well accepted that C_D is not constant and can present very different values according to spacecraft shape and the atmospheric temperature and composition at the flying altitude [11].

Ion thrusters are known to cause detrimental effects in the near-spacecraft environment related to propellent material deposition, optical and photovoltaic contamination, radio-frequency interactions, and spacecraft charging. Such effects are introduced primarily from plume charge-exchange (CEX) backflow and spacecraft charge interactions with the plume-induced plasma environment. The objective of this work is to assess whether these mechanisms modify the

properties of the thermospheric flow about VLEO satellites to have significant impact on the value of C_D. A detailed characterisation of the plume dynamics in VLEO is required to ensure that drag predictions are inclusive of plume interactions with the base-flow.

It is difficult to measure thruster plume backflows in near-vacuum space environments via ground chamber testing because of the presence of finite background pressure, and to replicate thermospheric freestream requires a hyperthermal wind tunnel. Therefore, the role of numerical simulations is important. Brieda et al. [12] studied ion thruster plume interactions and the role of CEX reactions using the PIC method. Additionally, the sensitivity of a thruster parameters in vacuum and chamber configurations was investigated to measure interactions at spacecraft surfaces. Stephani et al. [13] investigated interactions between the Space Shuttle Endeavour's reaction thruster plume and the ionosphere using a DSMC/PIC approach to characterise interactions of a neutral plume in a charged ambient freestream (the opposite physical system to this work). Finally, Wang et al. [14] performed simulations of ion thruster plume interactions to study spacecraft–plasma interactions on solar cell panels using PIC and immersed finite element techniques. An overlay method was used, with macro-parameter fields used to calculate the trace species flow-field properties, reducing the computational effort and the statistical scatter. However, the use of this assumption was seen to result in a 13% difference between the magnitude of velocity profiles of neutral species modelled with and without the inclusion of CEX collisions in the downstream plume. This difference is critical in understanding the influence of thermospheric species CEX collisions with beam ions.

Tumuklu and Levin [15] used the DSMC/PIC method to examine the effects of atomic oxygen (O) on ion thruster plume distributions. The effect of ambient atomic oxygen with different angles with respect to the thrust vector at two different altitudes was studied. It was found that the presence of the atomic oxygen modifies the backflow of Xenon (Xe), especially at 185km, which can be further ionised to cause additional contamination. However, there was no significant effect seen in the backflow of the Xe at 300km due to the lower density of O. It was also found that the Xe^+ fluxes scaled linearly with the ambient atomic oxygen concentration, such that the spatial distribution of fluxes at various altitudes can easily be scaled. Previous work by the authors [16,17,18] showed that, at altitudes up to 400km, ambient plasma flow around spherical satellites was affected by a combination of collisional and indirect electrostatic interactions in the presence of an ion thruster plume, but did not attempt to quantify the effects of the individual mechanisms or net effect on the body drag force. The primary ion beam was observed to act as a potential barrier to freestream ions, and that ions with enough energy to penetrate the plume led to a number of electrostatic instabilities in the plume/wake.

To accurately simulate the collisions between thermospheric and plume species, DSMC simulations require the elastic, momentum exchange (MEX) and the CEX collision cross sections. Levandier and Chiu [19] used collimated-ion beams to understand reactions of Xe^+ and Xe^{++} with ammonia under hyperthermal collision conditions. Bastian et al. [20] measured ambient $O^+ - Xe$ CEX collisions but not the reverse process required within this study. CEX in other molecular systems such as N_2 and Kr have also been measured and calculated [21], some of which are relevant to predicting collisional radiative models. However, there have been no experiments or empirical attempts to model the CEX between thermospheric species and Xe/Xe^+ at the energy levels of interest in this work. Korkut and Levin [22] investigated collision cross-section models between Xe^+ and O particles with the analytic approach of Rapp and Francis [23], where the resonant approximation was employed. The calculated cross section of the reverse CEX process was found to be in good agreement with the variable hard sphere model for $Xe - O$ elastic collisions for space environment conditions and was verified by comparison with the high-fidelity Lennard–Jones model [24].

This work presents coupled DSMC/PIC simulations of a steady-state drag-compensating ion thruster in the 160-250km VLEO range. The aim is to analyse the importance of direct thermospheric particles in the CEX, characterise the thruster plume backflow in the presence of the ambient flow, and the effect of such interactions on the spacecraft drag profile C_D. Section 2 will review the important aspects governing the DSMC/PIC method used in this work, and the implementation of a Poisson-switch in order to reduce the computational time whilst still correctly resolving the potential gradients in regions of low plasma density. Section 3 presents the models for collision cross sections, discussing the Variable Hard Sphere (VHS) approach and the theory of Rapp and Francis, required because the direct cross section between ambient thermospheric species and Xe/Xe^+ has not been measured or calculated using quantum approaches. Section 4 presents the numerical parameters of the thermosphere and plume, as well as simulation setup/topology. The results and a discussion of effects to the plume structure, plume interactions with the thermosphere and the effect on the satellite drag coefficient is given in section 5. Finally, the conclusions and thoughts toward future work are contained in section 6.

2. Direct Simulation Monte-Carlo/Particle-in-Cell

This section provides an overview of kinetic theory and the DSMC and PIC methods. For a detailed background and discussion of DSMC and PIC, the reader is referred to the works of Bird [25] and Birdsall [26] respectively. The SI system of units is used throughout this work unless other units are given. Freestream and surface temperatures are discussed in Kelvin, however plasma temperatures are referenced in electron-Volts (eV).

2.1 Kinetic Theory

The ion thruster plume plasma expands into the rarefied free-molecular thermosphere, where at altitudes greater than 160km the Knudsen number $Kn \gg 10$ and the continuum mechanics formulation of fluid dynamics is no longer valid. The thermosphere-plume system consists of neutral atoms and particles, positive ions and negative electrons. The spatial distribution function, in two-dimensions, of particles of species k is defined as $f_k(\boldsymbol{x}, \boldsymbol{c_k}, t)$ within the area element $dxdy$ where $\boldsymbol{c_k}$ and $\boldsymbol{x}$ are the particle velocity and position at time t. The evolution of f_k in t is determined by the Boltzmann equation

$$\frac{\partial f_k}{\partial t} + \boldsymbol{c_k} \cdot \boldsymbol{\nabla_x f_k} + \frac{\boldsymbol{F_k}}{\boldsymbol{m_k}} \cdot \boldsymbol{\nabla_c f_k} = \left(\frac{\partial f_k}{\partial t}\right)_{\boldsymbol{collisions}} \quad (2)$$

where, from left, the terms represent the rate of change of f_k with time, diffusion of f_k, external forces $\boldsymbol{F_k}$ acting on f_k and the rate of change of f_k due to direct particle collisions. In the neutral thermospheric freestream $\boldsymbol{F_k} = \boldsymbol{0}$. In the plume plasma, $\boldsymbol{F_k}$ describes the interaction of particles of mass m_k and charge q_k through their mutual electric $\boldsymbol{E}$ and magnetic $\boldsymbol{B}$ fields via the Lorentz force

$$\boldsymbol{F_k} = q_k(\boldsymbol{E}(\boldsymbol{x}, t) + \boldsymbol{c}_k \times \boldsymbol{B}_k(\boldsymbol{x}, t)) \quad (3)$$

For a gridded ion thruster, interactions are considered electrostatic and un-magnetised such that Maxwell's equations reduce to Poisson's equation for the electric potential Φ

$$\boldsymbol{E} = -\nabla\Phi, \quad \nabla^2\Phi = -\frac{\rho_c}{\epsilon_0} \quad (4)$$

where ϵ_0 is the permittivity of free space and ρ_c is the total macroscopic charge density from K total ion species

$$\rho_c = \sum_k^K q_k \int f_k d\boldsymbol{c}_k \quad (5)$$

Determining the general f_k of a multi-species system in the presence of external and self-consistent forces is the complex challenge posed by kinetic theory. Direct solutions to Equation 2 become intractable for large practical cases. Particle-kinetic methods, such as the DSMC and PIC, avoid solving the Boltzmann equation directly by simulating the microscopic interactions of 'macro-particles'.

2.2 Direct Simulation Monte-Carlo

Direct Simulation Monte-Carlo (DSMC), originally developed by Bird [25], is a discrete direct particle simulation method that provides a statistical approximation to the solution of f_k where the collision kernal $(\partial f_k/\partial t)_{\boldsymbol{collisions}}$ drives the evolution of f_k, i.e. the system is collision dominated. DSMC is time-marching and provides a probabilistic physical simulation of a gas flow by simultaneously following the motion of representative macro-particles, each representing a large number $(10^6 - 10^{12})$ of true atoms, molecules or ions, in the physical space. It applies the *particle chaos* assumption - *velocities of colliding particles are uncorrelated, and independent of position* [27]. The basis is the ad hoc assumption that particle motion and collisions are decoupled over a time-step Δt that is small in comparison with the Courant–Friedrichs–Lewy condition imposed by the mean free path.

During a DSMC time-step, macro-particles are moved ballistically over Δt . During the collision step, Markov processes describe the interaction of macro-particles according to kinetic theory and phenomenological collision models. Macro-particle motion can also be modified by including chemical reactions and gas-surface interaction with solid bodies.

The DSMC approach is based on the use of two separate meshes: a sampling and a collision mesh. The former samples the molecules' microscopic properties. In the more numerous collision cells, candidate collision pairs are selected from a sampling cell based on collision probabilities. Collision pairs then undergo an acceptance-rejection test. This work uses the No-Time-Counter (NTC) method of Boyd [28]. The basis of the NTC method lays in determining the differential scattering cross-section as discussed in section 3.

The macro-particle expedient reduces the computational requirements to a feasible level but also results in numerical fluctuations of macroscopic gas properties that are much larger than the physical fluctuations of the real gas. Macroscopic properties must therefore be sampled directly from the particle distribution by applying time-averaging.

2.3 Particle-in-Cell

The Particle-in-Cell (PIC) method [29] determines solutions to the Vlasov-Maxwell system where the contribution of collisions in Equation 2 are neglected, i.e. collective dominated systems. The numerical implementation of the PIC method is similar to the

DSMC method. Within the ion thruster plasma plume, Equation 2 becomes the electron momentum equation

$$\frac{\partial}{\partial t}(n_e m_e \boldsymbol{c}_e) + n_e m_e(\boldsymbol{c}_e \cdot \nabla_x)\boldsymbol{c}_e + q_e n_e(\mathbf{E} + \boldsymbol{c}_k \times \boldsymbol{B}_k) + \nabla_x p_e = n_e m_e \nu(\boldsymbol{c}_i - \boldsymbol{c}_e) \quad (6)$$

where $n_e$is the electron number density, p_e electron pressure, and ν the electron viscosity. Electrons respond near-instantaneously to any perturbance, thus transient terms are negligible and $\partial/\partial t = 0$. The advective term is also small and ignored. The friction term $n_e m_e \nu(\boldsymbol{c}_i - \boldsymbol{c}_e)$ arises from electron-ion collisions and can be removed for $\nu \to 0$. Since the plasma is meso-thermal $\boldsymbol{c}_e \gg \boldsymbol{c}_i$, $\boldsymbol{c}_i \approx 0$ can be assumed. Substitution of the ideal gas law $p_e = n_e k_B T_e$ can be made, assuming isothermality at T_e , where k_B is the Boltzmann constant. From the un-magnetised assumption stated in section 2.1, in the plume $\boldsymbol{B} = \mathbf{0}$, and since thrusters operate at sufficiently low current densities where $\partial \boldsymbol{B}/\partial t \approx 0$ this allows one to compute the electric field from a scalar plasma potential [30], as given previously in Equation 4, so Equation 6 reduces to the prominent Boltzmann relationship

$$n_e = n_0 exp\left(\frac{q_e(\Phi - \Phi_0)}{k_B T_e}\right) \quad (7)$$

It is substituted into the Poisson's equation (Equation 4) to give the following expression for plasma potential

$$\epsilon_0 \nabla^2 \Phi = -q_e\left(n_i - n_0 exp\left(\frac{\Phi - \Phi_0}{k_B T_e}\right)\right) \quad (8)$$

where n_i is the number density of positive ions.

2.4 Non-Linear Boltzmann Electron Fluid Model and Poisson Switch

In principle, it is possible to employ fully-kinetic PIC simulations, with both ions and electrons featuring as simulation macro-particles. Directly simulating electrons comes at significant computational cost, however. Δt must be smaller than the fastest plasma frequency ω_p. In a similar manner, the stability requirements of leapfrog integration requires a spatial discretisation of $\Delta x, \Delta y < \lambda_e/2$ where λ_e is the smallest Debye length. Fully kinetic simulations require artificial ion to electron mass ratios to reduce the difference between electron and ion time-steps. To model correctly a mesothermal plasma, an extremely large ratio would need to be used. By replacing the electron macro-particles with a fluid allows simulations to employ time-steps up to 10^6 times larger than the full kinetic. The benefits of a larger time step and reduction in simulated particles (no electrons) often outweighing the computational cost of solving, in this case, the non-linear Poisson's equation. For these reasons, there are significant computational cost reductions if a fluid can approximate the electron distribution.

A common assumption in ion thruster plume modelling is that of quasi-neutrality $(n_e \approx n_i \approx n)$, where the electron distribution function can be described by an isothermal, currentless (electrostatic), inertia-less $(m_e/m_i \to 0)$ Boltzmann fluid. The reference point for the electron density distribution is set to be at the thruster exit, resulting in a hybrid scheme in which only the heavier ions and neutrals are modelled with particles. The direct potential field is therefore acquired through inversion of Equation 5.

$$\Phi = \Phi_0 + \frac{k_B T_e}{q_e} \ln\left(\frac{n}{n_0}\right) \quad (9)$$

where Φ_0 is the plasma potential at the reference condition.

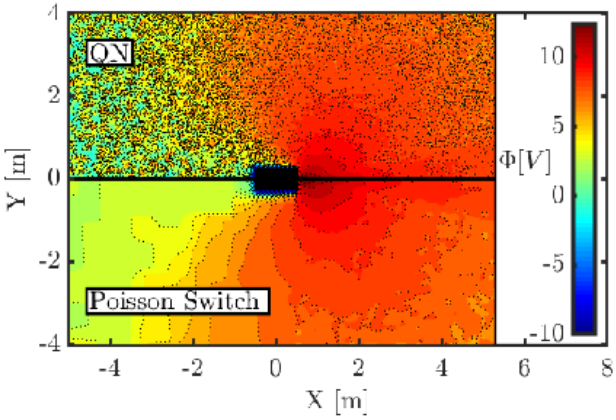

Fig.1. Comparison of electric potential solution Φ using pure Quasi-Neutral (QN) and the Poisson switch. The solution is identical in the plume region, but the switch solver also resolves the sheath around the negatively charged satellite and resolves the backflow region.

The quasi-neutral approach offers extremely rapid computation of plasma potential in the plume but does not correctly resolve potential drop in the non-neutral satellite sheath or low density CEX region. Passaro et. al. [31] report up to 15% under-prediction in charge density of gridded ion engine backflow regions. To address this, a combined "Poisson switch" method was developed, similar to that proposed by Santi and Cheng [32], and Brieda et. al. [33]. Prior to commencing the solver iterations, the local λ_D at each node of the simulation domain is calculated. If $\lambda_D^2 < \Delta x \Delta y$, the node was flagged as quasi-neutral and potential on it fixed to the value obtained by the direct inversion. The Poisson solver then backfills the remaining region using a second-order Gauss-Siedel regime. Comparison between the two solutions is shown in Figure 1. The plot was generated by injecting propellant particles for only $50\mu s$ to ensure

equal charge-density, thus the potential distribution is not at a steady-state. As seen, the solutions are identical in the plume region, as expected. The Poisson switch approach, however, correctly captures the satellite plasma sheath and resolves the backflow region. The pure quasi-neutral effectively compresses the sheath to the thickness given by a simulation cell. The ions are not aware of the satellite surfaces until they reach the cell adjacent to it. This difference has a profound implication on the trajectories of the CEX ions, trajectories of which are primarily influenced by the electric field between the plume and the satellite surface charge. It should be noted that a fully kinetic non-switched Poisson solver was not able to converge for the simulations in this work.

The DSMC-PIC used in this work was implemented via plugins within Starfish [34], a two-dimensional code for plasma and gas kinetics problems. It uses the PIC method to model plasmas, with multiple gas injection sources, and a detailed surface handler for gas-surface interactions. The species interact with each other via DSMC or Monte Carlo Collisions (MCC) or by chemical reactions. The trajectory of particles is integrated with a leap-frog method, putting velocity increments on the ions at each time-step

$$m_k \frac{d\boldsymbol{c}_k}{dt} = \boldsymbol{F}_k = q_k \boldsymbol{E}_k, \qquad \frac{d\boldsymbol{x}_k}{dt} = \boldsymbol{c}_k \tag{10}$$

3. Collision Dynamics and Associated Cross-Sections

The base-flow thermosphere-plume system under consideration can be considered as four species subsets: propellent neutrals/ions, which in this work is Xenon (Xe/Xe^+) and ambient thermospheric neutrals/ions, which shall be referred to generally as A/A^+. The ion thruster ejects a high-density collimated plume of quasi-neutral ions, which expands into the surrounding ambient flow. Unionised neutral propellent drifts across the thruster exit with pure thermal velocity. The thermospheric model used in this study is comprised of the primary species found in VLEO, atomic oxygen O, diatomic nitrogen N_2, diatomic oxygen O_2, atomic nitrogen N, argon Ar, helium He and atomic hydrogen H. The presence of charged ionospheric species is neglected.

The following interactions between neutrals and ions were modelled:

$$Xe_{(p_1)} + Xe_{(p_2)} \rightarrow Xe_{(\acute{p_1})} + Xe_{(\acute{p_2})} \tag{11}$$

$$Xe^+_{(p_1)} + Xe_{(p_2)} \rightarrow Xe^+_{(\acute{p_1})} + Xe_{(\acute{p_2})} \tag{12}$$

$$Xe^+_{(p_1)} + Xe_{(p_2)} \rightarrow Xe_{(p_1)} + Xe^+_{(p_2)} \tag{13}$$

$$A_{(p_1)} + A_{(p_2)} \rightarrow A_{(\acute{p_1})} + A_{(\acute{p_2})} \tag{14}$$

$$Xe_{(p_1)} + A_{(p_2)} \rightarrow Xe_{(\acute{p_1})} + A_{(\acute{p_2})} \tag{15}$$

$$Xe^+_{(p_1)} + A_{(p_2)} \rightarrow Xe^+_{(\acute{p_1})} + A_{(\acute{p_2})} \tag{16}$$

$$Xe^+_{(p_1)} + A_{(p_2)} \rightarrow Xe_{(p_1)} + A^+_{(p_2)} \tag{17}$$

where p_1 and p_2 are the pre-collisional momentum, and $\acute{p_1}$ and $\acute{p_2}$ are the post-collisional particle momentums. The A neutrals could participate in both momentum exchange (MEX) and CEX interactions, but the post-collision properties of A^+ were not updated. Both Xe and Xe^+ participate in MEX and CEX interactions. A summary of the permitted interactions for this chemical system are provided in Table 1. The rotational and vibrational internal structure of plume and ambient constituents is neglected.

Table 1. Permitted Interactions between Plume and Ambient Species

	Xe	Xe^+	A	A^+
Xe	MEX(8)*	MEX(9)/ CEX(10)	MEX(12)	-
Xe^+	-	-	MEX(13)/ CEX(14)	-
A	-	-	MEX(11)	
A^+	-	-	-	-

* Numbers in brackets refer to interaction equation above

3.1 Momentum Exchange Collisions

The elastic cross section is critical for accurately capturing the penetration and mixing of ambient species into the plume. The variable hard sphere (VHS) model [25, 27] was used to calculate neutral collision cross-sections σ_{VHS} as per standard dynamics of DSMC isotropic scattering, assuming inter-molecular forces remained negligible relative to the energy of the thermospheric and plume species. It should be noted that the average relative velocity between neutral Xe and ambient species for the collision conditions in this work is around 8000m/s or energies of 4.7eV. Comparison of the VHS model to the high-fidelity Leonard-Jones model in [15] showed very good agreement at 5eV for $Xe - O$ collisions. The VHS collision cross-section is given by

$$\sigma_{VHS} = \frac{\pi d^2_{REF}}{\Gamma(2.5-\omega)} \left[\frac{2T_{REF}k_B}{m_r g^2}\right]^{(\omega-0.5)} \tag{18}$$

where g is the relative speed, m_r is the reduced mass, and Γ is the gamma function. The viscosity index ω and the reference diameter d_{REF} are DSMC molecular gas properties taken at $T_{REF} = 273K$. For MEX collisions between unalike species, the greatest value of ω was

used and d_{REF} interpolated the intermolecular distances of individual particles. Figure 2 illustrates that σ_{VHS} is maximum at zero energy and decreases with increasing energy due to decreased interaction time. Most probable collisions between plume constituents and the incoming thermosphere are with N_2 and H. N_2 is one of the most concentrated species in VLEO (the other being O), therefore N_2 is likely to have the most significant impact on the plume structure and modification to the base-flow. The density of H is $O(10^5)$ lower. Note that MEX cross-sections for $Xe - A$ and $Xe^+ - A$ are considered equivalent.

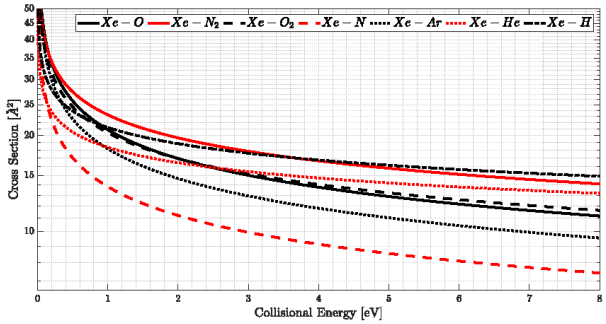

Fig. 2. Variation of VHS Collision Cross-Section with Collisional Energy for $Xe - A$ (Equation 12) Momentum Exchange Collisions

The total number of candidate collision partners within a cell is then determined with the NTC. The probability P_{MEX} of a collision event is determined for candidate pairs based on the total collision cross section.

$$P_{MEX} = \frac{\sigma_{VHS} \cdot g}{(\sigma_{VHS} \cdot g)_{max}} \tag{19}$$

where a candidate pair is selected for collision if $P_{MEX} > \mathbb{R}_u$, in which $\mathbb{R}_u$ is a uniformly distributed random number.

3.2 Charge-Exchange Collisions

Charge-exchange (CEX) is a process which occurs when outer electron shells of a neutral atom and ion collide, resulting in electron transfer from the atom to the ion [35]. CEX collisions were modelled using the Monte-Carlo-Collision (MCC) method [26], which differs from DSMC in that source particles are collided with a target cloud of neutrals, which does not have its properties updated. In the thruster exit region, the number density of unionised propellent and thermospheric species are of order $O(10^{17})$, whereas that of primary beam ions is $O(10^{15})$. Therefore, it was considered reasonable to assume that neutral species were affected by collisions to such a small extent that the gross distribution was undisturbed, and the MCC method valid. Since MCC does not require particle tracking of neutrals within the collisions, the computational expense is greatly reduced.

The CEX process in ion thruster plumes of Equation 11 is well understood from multiple experiments of $Xe - Xe^+$ bombardment [19,20,23]. Analysis by Boyd and Dressler [36] and experimental measurements by Pullins and Miller et. al. [37] has demonstrated that the $Xe - Xe^+$ CEX cross-section is approximately equivalent to the non-resonant MEX cross-section, i.e. $\sigma_{CEX} \approx \sigma_{VHS}$, even though Figure 2 shows that, on a linear scale, there is a difference in the resonant magnitudes. This relationship was assumed true and, if the collision under consideration involved a $Xe - Xe^+$, the probability of a CEX event was therefore taken to be 0.5 of the elastic collision probability, $P_{CEX} = 0.5P_{MEX}$. In the resonant case, the cross section is, like the MEX process maximum at zero energy and decreases with increasing energy, as given in Figure 3 as a function of the relative speed.

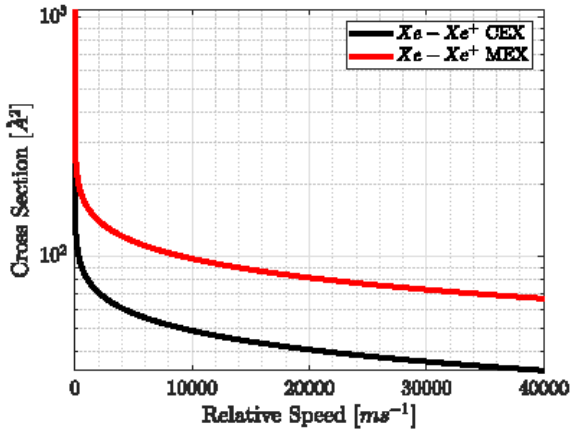

Fig. 3. Variation of Resonant MEX and CEX $Xe - Xe^+$ Cross-Section with the Relative Speed

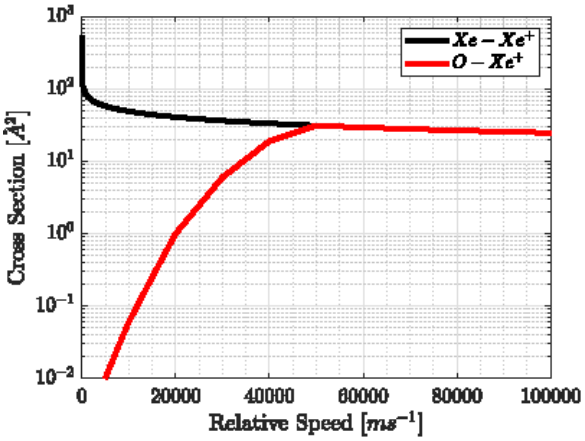

Fig. 4. Comparison of $O - Xe^+$ Cross-Section for Non-Resonant Case with the Relative Speed

The differential cross-section for CEX collisions between Xe^+ and thermospheric species have not been measured in previous works, thus the approach of [38] was used to infer the values. The reacting species were

assumed to be in ground states; a reasonable assumption, as plasmas in ion thrusters have characteristically cold ions with high electron to ion temperature ratios ($T_e/T_i \approx 10$), resulting in a 96% Xe^+ population in the ground electronic state. Thermosphere species never exceed total temperatures of approximately 0.1eV. Resonant and near-resonant CEX occurs when the ionisation potentials of colliding species are similar, and the energy difference between collision pairs before and after a CEX collision, the defect energy ΔE is near-zero. CEX cannot occur at collision energies lower than ΔE, and in this case the collision was modelled as MEX. In the MCC routine, the collisional energy was calculated and, if $\Delta E < 0$, collisions were handled by the DSMC routine. Else, for $\Delta E \geq 0$, the CEX was modelled, with the maximum CEX cross section estimated with the relation reported by Sack et. al. [39]

$$\sigma_{\mathrm{CEX}} \cong \begin{cases} \frac{10.8h^4}{\pi}\frac{E_B g^4}{R_\infty a_0^2 \Delta E^4}, & \text{if } \Delta \mathrm{E} \geq 0 \\ \approx 0, & \text{if } \Delta \mathrm{E} < 0 \end{cases} \quad (20)$$

where a_0 and E_B are the Bohr radius and the ionisation potential of the neutral, h Planck's constant and R_∞ the Rydberg constant. This approach for $Xe^+ - O$ has shown good agreement with the resonant cases of $O^+ - O$ collisions by Lindsey et. al. and the experiments of the reverse interaction $O^+ - Xe$ made by Bastian et. al. [20].

As example, to calculate the CEX cross-section of $Xe^+ - O$, Equation 20 with ionisation potential of O $E_B = 13.6$eV was used in the region where the relative speed is less than $50000 ms^{-1}$, whereas above this, it was approximated as that of $Xe^+ - Xe$. With this approach, Figure 4 shows the CEX cross-section between the $Xe^+ - O$ pair as a function of relative speed. There was no data readily available to compare laboratory measurements of CEX processes of thermospheric species other than O.

4. DSMC/PIC Flow Conditions and Numerical Parameters

4.1 Very Low Earth Orbit Thermosphere

There exists no standard definition of VLEO, with previous literature quoting various ranges between 60-450km [1-5,7-9]. The definition adopted here is that VLEO refers to 160-250km. This arises from the fact that below 250km, the aerodynamic drag becomes the dominating orbital perturbation (over 250km it is the perturbation of lunar gravity), and 160km represents the Kármán line where it is internationally agreed to be the boundary between atmosphere and the space environment.

Thermospheric conditions in VLEO were modelled using data from the NRLMSISE-00 Standard Atmosphere Model [40]. This model provides total temperature and gas species number densities for O, N_2, O_2, N, Ar, He and H covering altitudes from sea level up to the exosphere. It accounts for the contribution of non-thermosphere species to the drag at high altitudes, such as O^+ and energetic oxygen atoms resulting from photochemical processes in the upper atmosphere, by including a component named 'anomalous oxygen'. The properties of the thermosphere are not uniform, varying with the solar cycle as well as the Earth's ground topology and other local irregularities. Thus, over a single VLEO orbit, the density and composition of the environment varies significantly. For this work, a spherical average density, temperature and composition was calculated for NRLMSISE-00 data at 00:00:00 01 March 2000, the peak of the last active solar maximum, with $F10.7_{Ave} = 219.38 sfu$ and $F10.7 = 214.70 sfu$, and $Ap = 21$. The resulting profile is given in Figures 5 and 6 for number density and neutral temperature respectively. The increased atmospheric density and temperature at these conditions represents a worst-case for satellite drag.

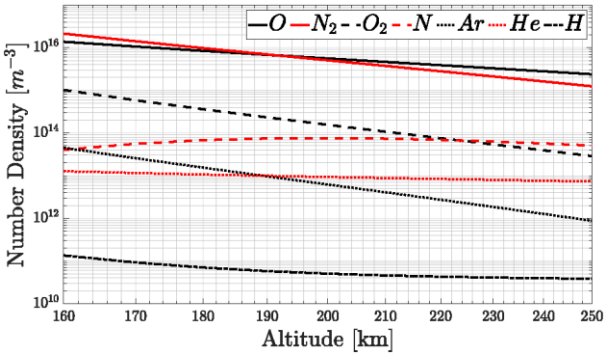

Fig. 5. Thermospheric Composition by Species in VLEO: Extreme Solar Maximum NRLMSISE-00 00:00:00 01/04/2000 $F10.7 = 219.8$ $F10.7_{Avg.} = 214.7$ $Ap = 21$

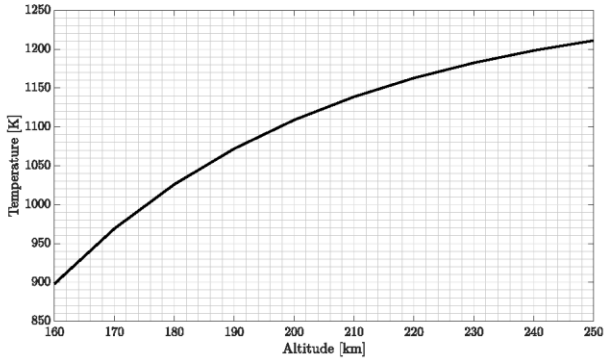

Fig. 6. Neutral Thermospheric Temperature in VLEO: Extreme Solar Maximum NRLMSISE-00 00:00:00 01/04/2000 F10.7 = 219.8 $F10.7_{\mathrm{Avg.}} = 214.7$ Ap = 21

4.2 Ion Thruster Plume

The propulsion device modelled in this study is the 10cm-diameter Qinetiq T5(UK-10) ion thruster, with an input power range of 50-660W [41]. The propellent Xe^+ ions are accelerated through ion optic grids to form a beam with voltage V_b up to 1100V, producing exhaust velocities v_e up to $40000ms^{-1}$. Measurements have shown that the Xe^+ ions form a divergent beam with a half-angle of about 14° due to curvature of the exit grid and chamber wall effects [42]. The ion beam is kept quasi-neutral by electrons emitted from a neutralising cathode. The density of the neutral plume remains quasi-steady due to the low CEX collision rate. One can estimate average neutral density at the thruster exit n_{n0} from the main flow rate, cathode flow rate, and the propellant ionisation efficiency η_i.

$$n_{n0} = \dot{n_0}/\left(A_e\sqrt{8k_BT_w/\pi m_{Xe}}\right) \tag{21}$$

where $\dot{n_0}$ is the number flow rate at the exit, A_e is the thruster exit area and $m_{Xe} = 131.4amu$, the Xe^+ ion mass. CEX collisions occur between the beam ions and the neutrals. The average CEX ion production rate at the thruster exit dn_{cex0}/dt is given by

$$\frac{dn_{cex0}}{dt} = n_{b0}n_{n0}v_e\sigma_{CEX} \tag{22}$$

Where n_{b0} is the average Xe^+ beam ion density at the thruster exit and σ_{cex} the $Xe - Xe^+$ CEX collision cross-section from section 3.2 taken at v_e. These set the reference conditions for the PIC solver.

4.3 Thruster Operating Parameters and GOCE In-Flight Data

The T5 has a thrust range of 0.2-26.5mN, at a resolution of 12μN. There is no unique solution to the relationship between specific thrust and the associated values of thruster control parameters: magnetic field strength in the discharge chamber, anode current and discharge chamber Xe flowrate. This study therefore produces a performance map of primary beam exhaust velocity v_e, given in Figure 7, mass flowrate $\dot{m}$, given in Figure 8, from data recorded from the GOCE ion propulsion assembly during its first 22 months of operation [43]. Note that in Figure 8, the mass flow rate at zero thrust is not itself zero due to a constant 0.2mg/s propellent flow through the cathode η_i was taken to be

$$\eta_i = 0.188ln(T) + 0.309 \tag{23}$$

as per the observations of Mundy and Fearn [44], where T is the thrust.

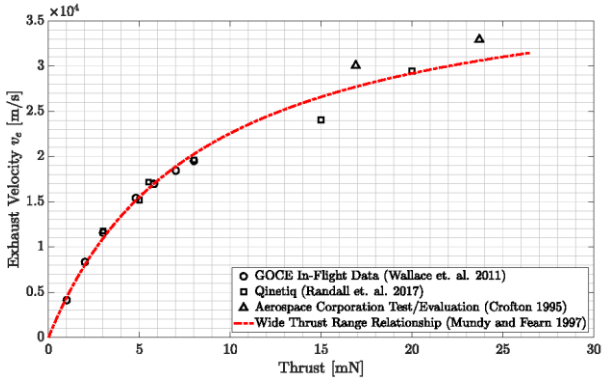

Fig. 7. Specific Impulse for Baseline T-5 Operating Parameters

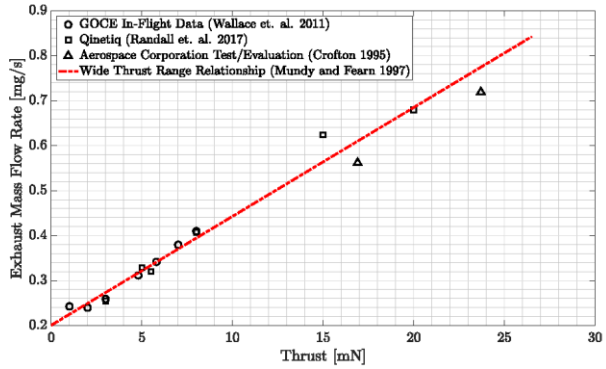

Fig. 8. Exhaust Mass Flow Rate for Baseline T-5 Operating Parameters

As the ion thruster onboard GOCE operated at a maximum thrust of 20.6mN, data from the ground-based experiments of Mundy and Fearn [44], Randall [45], and Crofton [46] is used to map performance up to maximum rated thrust. The T5 operates with a main flowrate of 0.25-0.842mg/s, for exhaust velocities approximately 2000-33700m/s, and ionisation efficiencies 5-95% for the thrusts required between 250-160km in VLEO. Using this data and the known thrust required to offset a given drag, it is possible to readily calculate n_{b0}, n_{n0}, and dn_{cex0}/dt near the thruster exit for each operating condition.

4.3 Computational Setup

Simulations were performed for 10km increments between 160-250km. At each altitude, simulations were performed for three cases:

- A clean satellite in absence of the ion thruster.
- The ion thruster plume at an operating condition equating the net drag in VLEO.
- The plume plasma expanding into a static vacuum environment for each equivalent thrust configuration.

The satellite geometry considered in this work was consistent with that examined by Walsh and Berthoud [8].

The satellite is considered a square prism of 1.00m length and 0.5m width, thus a frontal area of $A_f = 0.25m^2$ is presented to the oncoming flow. The T-5 propulsion assembly is assumed to be a cylinder centred on the aft satellite surface, with length 0.05m and radius 0.05m.

The satellite surfaces were taken to be isotopically conducting and the floating potential fixed at $\phi_{S/C} = -10V$ to approximate spacecraft charging in VLEO. During normal operation, electron emission keeps the exhaust plume quasi-neutral and prevents the spacecraft from charging up significantly. The surface temperature was considered to be uniform at $T_{S/C} = 490K$. It was assumed that photovoltaic arrays will be body-mounted, since the additional drag from array-mounted panels would likely make compensation in VLEO infeasible. The front face of solar arrays are typically covered by glass and thus insulators. The surface potential can therefore be taken to be approximately that of the surrounding electrons in the flow.

Gas-surface interactions were assumed to be diffuse with complete thermal accommodation to the satellite walls at $490K$, i.e. the coefficient of thermal accommodation $\alpha_T = 1$. In VLEO, as the surface contamination and mass of the adsorbed molecules increase, the angular distribution progresses from partly quasi-specular to fully diffuse. The surface material was represented as generic paint or solar-cell protection with surface molecular mass of 75amu.

The simulation domain is illustrated in Figure 9. The domain extends $-5 \leq x \leq 8\,m$ and $0 \leq y \leq 4\,m$, with the satellite centred at 0,0. The half-satellite thus located at $-0.5 \leq x \leq 0.5\,m$ and $0 \leq y \leq 0.25\,m$. The thruster exit grid is located at $x = 0.55m$, $0 \leq y \leq 0.05\,m$, and generates thrust in the $-x$ direction, such that the plume expands in the $+x$ direction. The simulations were performed as half-domain symmetric models of the satellite cross-section, given both the thermosphere and plume are axis-symmetric in the x-axis (asymmetry due to an off-axis neutraliser is considered negligible in the far field).

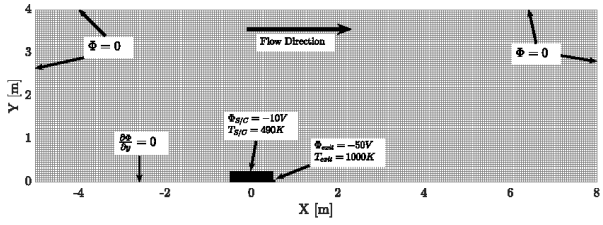

Fig. 9. Simulation Domain with Annotated Boundary Conditions. Every 5^{th} Mesh Node is shown for Clarity

The ion thruster Xe and Xe^+ species are injected into the domain at the thruster exit at each time step. The Xe^+ ions follow a Maxwellian distribution with mass flow rate and exhaust velocity prescribed by the T5 operating conditions in section 4.3, with isotropic fixed temperature of $T_{e,0} = 2.09eV$. The unionised Xe propellent was injected as a half-Maxwellian with only thermal speed (zero drift velocity) corresponding to the thruster wall temperature of $T_w = 250K$, at a mass flow rate given by the corresponding ionisation efficiency at the operating thrust. Freestream thermosphere enters the domain at the left-hand boundary in the $+x$ direction with a Maxwellian distribution according to the ambient total temperature T_a and drift velocity of the circular orbital velocity at the given altitude $\boldsymbol{v_{rel}}$. The reference frame is that in respect to a stationary spacecraft. Hence the satellite sees a thermosphere with relative velocity $\boldsymbol{v_{rel}}$ and a plume with relative velocity $\boldsymbol{v_{rel} + v_{plume}}$.

Symmetry was enforced at the x-axis by setting zero electric field in the normal direction $\partial\Phi/\partial y = 0$. A Dirichlet boundary $\Phi_{exit} = -50V$ was applied at the thruster exit as per the exit grid potential with temperature $1000K$. The upstream and downstream regions corresponded to the freestream reference and $\Phi = 0V$ was set on the left, top and right-hand boundaries. For the quasi-neutral inversion $\Phi_0 = 19V$ and $n_0 = n_{b0}$ varied with altitude, derived as per section 4.2.

To resolve the mean free path of collisions, mesh spacing was $\Delta x = \Delta y = 0.01m$, which required a time-step of $1.2 \times 10^{-6}s$ to ensure that each species did not traverse multiple collision cells in a single time-step. The simulations were run for a total of 50,000 time-steps and were sampled for the last 15,000 time-steps. Each simulation contained approximately 1.2 million Xe and Xe^+ macroparticles, and 500000 of each thermospheric species, to obtain a steady-state flow-field independent of any numerical parameters. The drag force was calculated by directly summing the momentum lost by particles impacting the satellite surface at each time-step. An initial value of thrust was set as equal to the clean satellite drag, calculated from simulations in absence of the thruster. Since the presence of the plume was theorised to change the gross drag, at every 1000^{th} time-step the thruster exhaust parameters were updated such to reset the thrust equal to the drag measured at that time-step in the simulation. All simulations converged to an equilibrium drag-compensating thrust before 35000 time-steps. The wall-clock time required to run each case was 7-29hr on 16 2.6GHz cores of the BlueCrystal Phase 3 supercomputing cluster, run by the High Performance Computing Centre at the University of Bristol.

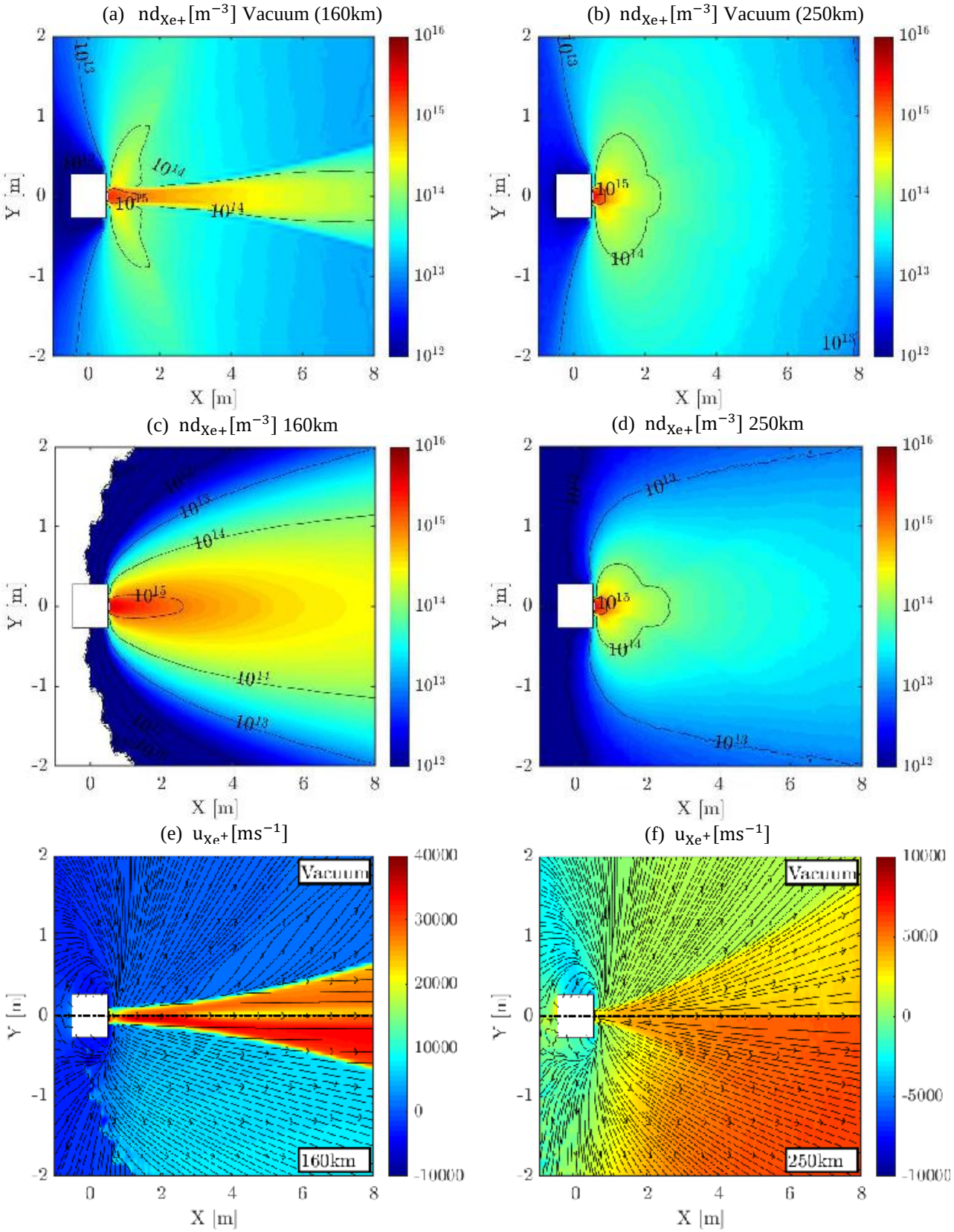

Fig. 10. Enlarged thruster plume structure results: number densities of (a) Xe^+ ions in the vacuum case at the equivalent 160km thrust condition, (b) Xe^+ ions in the vacuum case at the equivalent 250km thrust condition, (c) Xe^+ ions at 160km VLEO, (d) Xe^+ ions at 250km VLEO, and x-velocity field with streamlines for (e) vacuum and 160km, and (f) vacuum and 250km

5. Results and Discussion

Although simulations were conducted for 10km increments in VLEO, the results here are presented with spatial distributions of flow macro-parameters for 160km and 250km only, as it would be infeasible to discuss each altitude within the scope of this paper.

5.1 Ion Thruster Plume Structure in the Thermosphere

5.1.1 Xe^+ Number Density

Figures 10 shows the spatial distribution of Xe^+ number density and velocity in the ion thruster plume for a drag-compensating thruster at 160km and 250km in VLEO, compared to the equivalent operating condition in a vacuum environment, i.e. in absence of the thermosphere. The number density contour levels are distributed exponentially to highlight the difference in concentration of the plume in the far field. In the velocity fields in Figures 10e/f, streamlines are observed to curve toward the +x-direction in presence of the thermosphere, tending to the drifting Maxwellian of the freestream with drifting velocity $0.9\,\boldsymbol{v_{rel}}$ at 160km and $0.79\,\boldsymbol{v_{rel}}$ at 250km. This indicates that the low-energy CEX ions are partially "picked up" by the thermosphere. This occurs because the relative speed of CEX ions is relatively low with respect to the freestream in this region, such that the number of collisions between Xe^+ and thermospheric species, predominately observed as $N_2 - Xe^+$, is sufficient to change the plume structure.

As CEX ions move downstream at 160km, those with sufficient energies re-enter the primary ion beam, and thus the beam retains greater streamwise number density over the vacuum case as it expands. CEX ions are influenced less by beam Lorentz forces as they gain energy/momentum from thermospheric collisions. Figure 10c illustrates how the plume therefore exhibits a Gaussian expansion beyond the boundaries of the primary beam, absent of the nominal CEX 'wings' seen in Figure 10a, as the primary ions and CEX ions merge into a continuous non-collimated structure.

The ambient thermospheric density at 250km is $O(10)$ lower than that at 160km, and the relative speed of CEX ions with respect to the incoming thermosphere increases approximately by 1km/s, reducing collision probabilities in the CEX cloud. The CEX ion production rate is also a magnitude greater near the thruster exit. The interaction of the thermosphere with the plume therefore decreases significantly as thermospheric species are unable to penetrate it. From Figure 10d, the CEX cloud retains its structure as it propagates downstream, but decreases in its crossflow dimension, before it is sufficiently rarefied that the primary and CEX ions become mixed. In a region approximately three exit-radii from the thruster centre, the Xe^+ distribution was seen to be unchanged.

To establish a relationship between altitude and back-flow Xe^+ flux density, the values at two different locations, the satellite fore-corner and aft-corner, in the back-flow region are shown in Table 2. Note that at the satellite fore-corner, the Xe^+ flux is zero at 160km, as the flow does not propagate upstream beyond half the satellite length, and changes sign (+) at 250km, because it is scattered by thermospheric species in the backward direction. The ambient density at 250km, however, is too low to see such mitigation of back-flow, although the back-flow is still impeded over the vacuum case. The aft-corner fluxes scale linearly with thermosphere concentration. At both altitudes, the average backflow number density can be observed to be reduced by $O(10^2)$.

Table 2. Xe^+ Fluxes at Satellite Fore-Corner and Aft-Corner in Thermosphere

	Xe^+ Number Flux $[m^{-3}s^{-1}]$	
Altitude [km]	x=0.5m,y=0.25m (Aft-Corner)	x=-0.5m,y=0.25m (Fore-Corner)
160	-5.64×10^{16}	0
250	-7.78×10^{16}	1.20×10^{15}

5.1.2 Xe Number Density

The spatial distribution of Xe number density is given in Figure 11. Since the neutral Xe drifts from the thruster exit, streamwise velocity is approximately $250ms^{-1}$ and the relative collision speed with respect to the incoming thermosphere $< 7.5kms^{-1}$, resulting in far greater collision occurrences between $A - Xe$ than $A - Xe^+$. However, the concentration of Xe is $O(10)$ greater than that of Xe^+ in the near-exit region and therefore the structure of the neutral plume is affected to a much smaller extent. The drifting Maxwellian distribution is modified from a vacuum case drifting speed of $250ms^{-1}$ to $0.12\boldsymbol{v_{rel}}$ at 160km and $0.45\boldsymbol{v_{rel}}$ at 250km.

The expansion fan of Xe backflow is largely unchanged at 250km, as shown in Figure 11b, although quantitative differences do exist, and reduction in number density reduces only far upstream of the satellite, where Xe concentration is sufficiently low to permit flow reversal. At 160km, Figure 11a, the Xe backflow density at the fore-corner is seen to drop by $O(10)$ over the vacuum case; the backflow is sufficiently weak that a propellent wake is formed in-front of the satellite.

5.2 Satellite Base-Flow Interactions with Ion Thruster Plume

The Mach contours for the aggregate thermospheric flow $(O, N_2, N, O_2, He, Ar, H)$ are given in Figure 12a/b, showing that, absent of the thruster, the flow undergoes significant changes. A significant diffusion of the effective bow shock in front of the satellite with increasing altitude is observed. Furthermore, Figure 12b

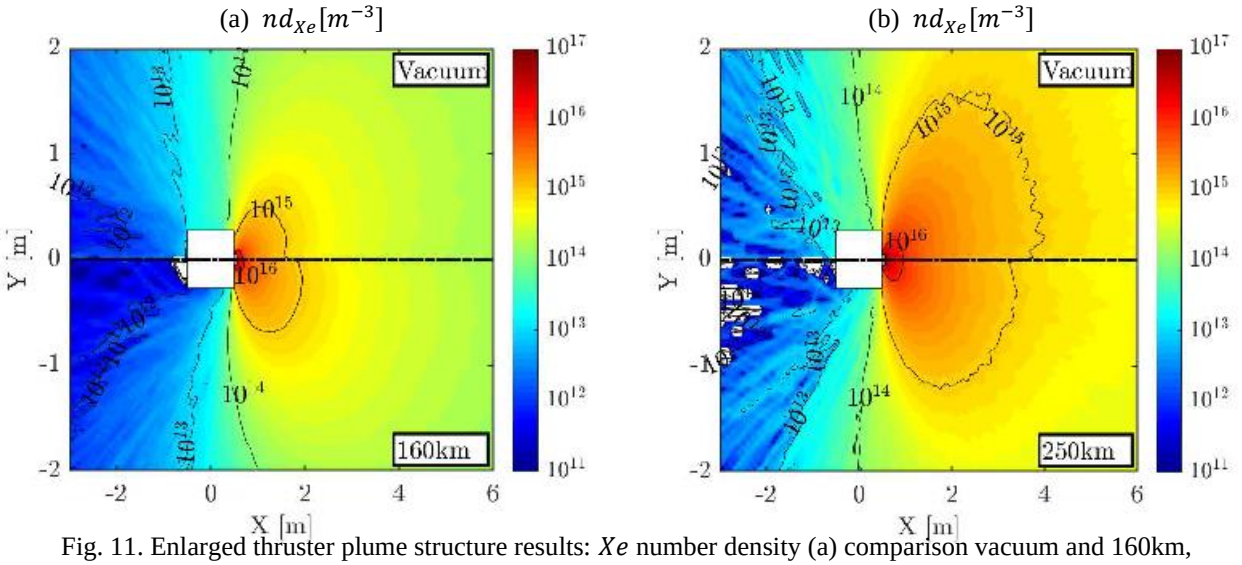

Fig. 11. Enlarged thruster plume structure results: Xe number density (a) comparison vacuum and 160km, and (b) comparison of vacuum and 250km

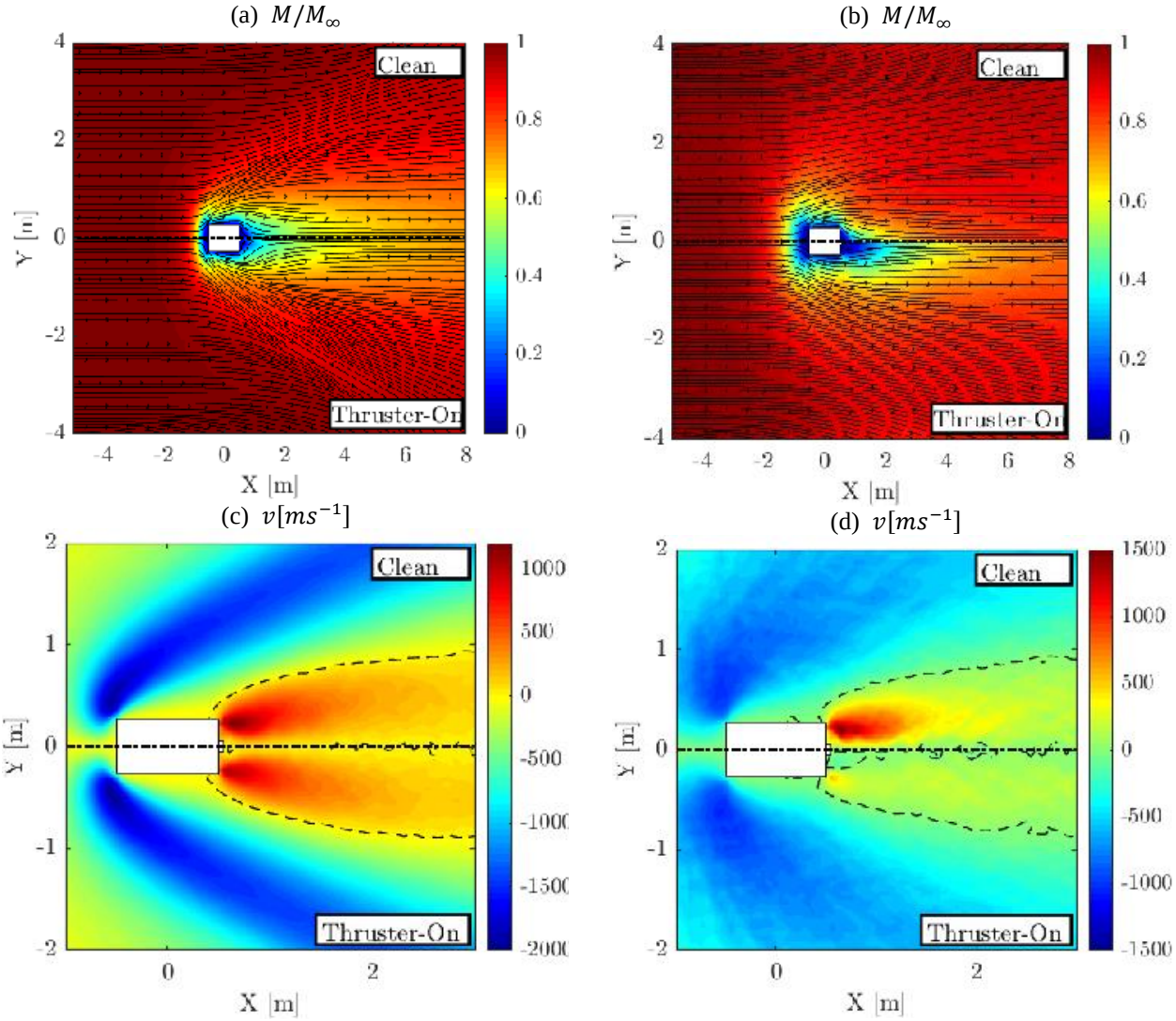

Fig. 12. Mach isolines for clean vs drag-compensating thruster-on condition, for (a) 160km, and (b) 250km, and vertical velocity (+ve toward centreline) for (c) 160km and (d) 250km. Black dashed line indicates zero cross-flow velocity

shows that at 250km, the isolines assume a more circular pattern throughout the flow-field, centred on the satellite body, and the downstream pressure recovery occurs in a less extended region with a resulting shortened shear. As altitude increases, the thermosphere becomes increasingly hyperthermal, reducing the molecular Mach angle and the degree of rarefaction in the flow, with most particles impacting the forward-facing surface only. At 160km the flow is near-transitional, but at 250km the Knudsen number approaches the order of $O(10^2)$ and the gas tends to the behaviour of the collision-less Boltzmann distribution.

Presence of the CEX plume delays the velocity recovery in the satellite wake as collisions between thermospheric species and plume constituents mean not all particles can penetrate to permit wake re-fill. At 160km the greater atmospheric density relative to the plume and decreased interaction time leads to greater modification to the plume structure by the thermosphere than vice versa, thus the wake region is nearly-identical to the clean case. At 250km, the plume density in the CEX cloud is greater than the ambient thermosphere and thermospheric species cannot easily penetrate the plume. The thermospheric freestream is therefore deflected around the structure of the plume and the wake extends downstream until the plume is sufficiently rarefied to allow the thermosphere to mix. The cross-flow dimension of the wake is increased to the order of 3 satellite widths over the clean configuration in which the wake does not extend beyond the satellite aft-corner.

The effect on the refill rate is clearly seen in the spatial distribution of vertical velocity in Figures 12c/d for the enlarged region about the satellite. Re-fill is significantly less at 250km than 160km. However, the zero cross-flow velocity contour, which originates at the aft corner, was seen not to vary spatially compared to the clean case. As the altitude increases, a high-pressure region immediately aft of the thruster exit increases in size shown by the growth of a second zero cross-flow contour. This represents the region where the coupled structure of the primary beam and CEX Xe^+ ions have sufficient density and radial velocity to reverse the direction of the thermospheric species which were able to penetrate the outer plume prior. Refilling thermopshere species enter a narrow wake structure bounded by the cross-flow equilibrium contours, at which the flow will be reflected in its radial velocity back into this structure. At 250km, Figure 12d shows that the penetration of the freestream is so weak that the result of the reflection is that the aggregate flow inside the narrow wake has near-zero velocity throughout.

5.3 Coefficient of Drag

The coefficient of drag was calculated by summing the total momentum lost by particles impacting the satellite surfaces over each time-step. The clean satellite drag profile, shown in Figure 13, is consistent with the results of Walsh and Berthoud [8] from the established DSMC program DS2V [27]. C_D was found to be 2.38 at 160km, increasing to 2.49 at 250km. Despite lower values of drag at greater Knudsen number due to the lower number of molecules impacting the satellite surface, higher values of C_D are found, as a consequence of the greater relative decrease with the altitude of both ρ_∞ and $\boldsymbol{v_{rel}}$; C_D therefore increases inversely proportional to the effective dynamic pressure.

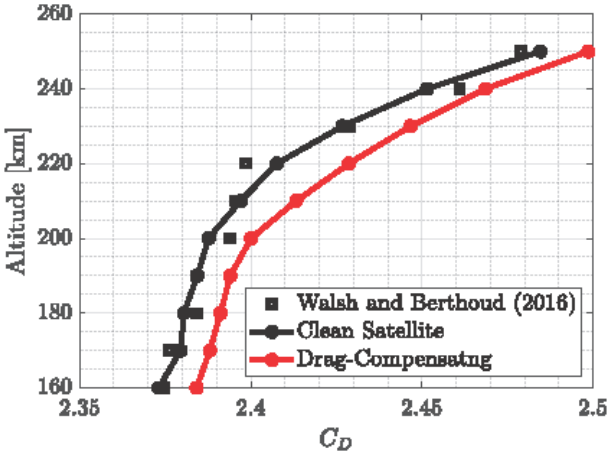

Fig. 13. Variation of Drag Coefficient with Altitude

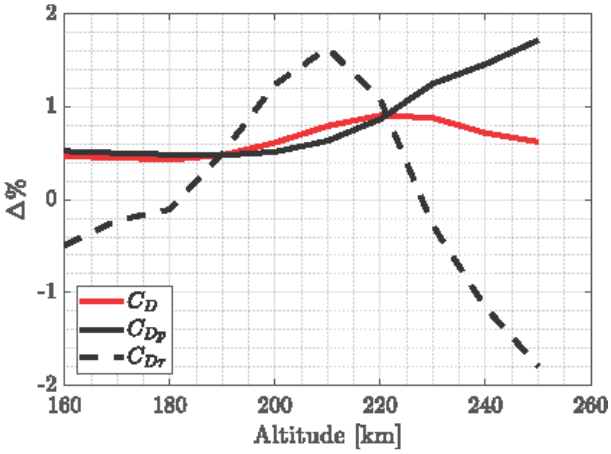

Fig 14. Percent Change in the Components of Drag Coefficient with Altitude

Figure 13 also shows the drag profile for the drag-compensating satellite with thruster. The drag coefficient was greater than the clean case at all altitudes, with C_D 2.385 compared to 2.376 at 160km, and up to a maximum of 2.501 from 2.486 at 250km. Figure 12 plots the percentage difference between the drag-compensated thruster-on and clean case, defined as $\Delta\% = 100(C_{Dthruster} - C_{Dclean})/C_{Dclean}$. The drag coefficient was 0.48% greater at 160km, but the difference reduces to 0.45% at 190km, before increasing to a plateau of

0.86% at 220-230km before reducing to 0.64% at 250km. The relative contribution of the pressure drag coefficient C_{Dp} and shear-stress drag coefficient $C_{D\tau}$ is also illustrated in Figure 12. Difference in C_{Dp} linearly reduces from 0.52% to 0.49% at 190km as the increasing concentration of the CEX structure serves to fill the wake. But the difference then rapidly increases to 1.72% at 250km as the CEX cloud is of sufficient strength to deflect the thermosphere about it, but not of the density required to fill the wake; therefore, the wake is greatly lengthened.

The variation in shear stress difference is more profound; at 160km the shear stress is reduced over the clean case by -0.49%, but rapidly rises up to a 1.63% increase on the clean at 210km. The difference reduces at approximately the inverse rate of the initial rise down to -1.79\% at 250km. This occurs according to the relative difference in the plume backflow flux and the freestream flux near the satellite top surface. At low-altitude the thermosphere is sufficiently dense, and at high-altitude the CEX region is sufficiently dense, for collisions with backflow propellent to reduce the velocity of incoming thermospheric species near the surface, whilst still allowing the majority of thermosphere to penetrate. This reduces the tangential momentum exchange at the aft of the satellite top surface and thus shear stress. Near 210km, the CEX region is dense enough to result in numerous collisions with the incoming thermosphere but the thermosphere is not of the necessary concentration to penetrate into the wake. High number density therefore builds up on the satellite top surface and shear stress increased.

The drag coefficient in the drag-compensating case is ultimately a function of the relative difference between the thermospheric and plume density, as well as the CEX ion production rate. With increasing altitude, the thermospheric density reduces exponentially and the CEX ion production rate increases logarithmically.

6. Conclusions

This work has presented a detailed analysis of satellite-plume interactions in a VLEO drag-compensation mission, which has been carried out with hybrid DSMC-PIC simulations inclusive of a refined collision model upon that found in the literature. The effects of such interactions were evaluated in the context of the satellite drag coefficient C_D. The following conclusions can be drawn.

Firstly, the Xe^+ and Xe back-flow is greatly reduced over vacuum cases and scales linearly with the ambient thermospheric density. Secondly, the wake refill is delayed due to collisions between CEX ions and thermospheric species, proportional to the relative difference between the ambient number density and the concentration of the near-exit CEX structure. The CEX cloud is partially picked-up by the thermosphere and propagates downstream.

C_D inclusive of thruster interactions was seen to be greater at all altitudes in the VLEO range, up to 0.86% larger at 220-230km. This is driven by an overall increase in pressure drag as the near-exit plume structure is of sufficient density to deflect the freestream but not to account for wake refill, and shear stress variation according to the collisions between plume backflow and thermospheric species, at parallel satellite surfaces, reducing the incoming velocity and increasing local density. Although the increase appears small, such an increase in drag accumulates over the mission such that the satellite re-entry may be many days prior to original estimates. This study has shown that effects of ion thruster interactions in VLEO should be included in future analyses, to ensure drag models are complete and accurate delta-V budgets are made.

It is also prudent to state that with the reduction in plume back-flow observed in the thermosphere, the usual detrimental effects associated with CEX ion-spacecraft interactions (recombination, charging, erosion) are of lesser concern. The use of a satellite surface potential of -10V may have been a conservative assumption, and the true charge in VLEO may be considerably less, decreasing the strength of the plume-to-satellite plasma sheath and reducing back-flow further.

Finally, future work shall focus on addressing the effects of some phenomena and mission features that have not been included in this study, such as: (I) different satellite geometries, (II) Earth magnetic field (affecting the plasma plume expansion), (III) self-consistent surface charging and (IV) different thruster models (including air-breathing and Hall effect thrusters).

Acknowledgements

The authors would like to thank Mr. Jonathan Walsh and Dr. Daniel Poole, University of Bristol, as well as Dr. Lubos Brieda, Particle-in-Cell Consulting LLC., for their assistance in this work.

The authors thank the European Space Agency (ESA) Education Office and the International Space Education Board (ISEB) for providing funding to attend this 70th IAC through the ESA/ISEB IAC Student Participation Programme 2019.

References

[1] D. G. Fearn, "Economical Remote Sensing from a Low Altitude", Acta Astronautica, vol, 56, no. 5, pp. 555-572, 2005.

[2] J. V. Llop, P. Roberts, Z. Hao, L. R. Tomas and V. Beauplet, "Very Low Earth Orbit mission concepts for Earth Observation: Benefits and challenges", Reinventing Space Conference, London, 2014.

[3] A. Green, “An Ultra Low Altitude Synthetic Aperture Radar Micro-Satellite”, University of Bristol Master’s thesis, 2012.

[4] A. Grasso, “Feasibility Study of an Ultra-Low Altitude Hyperspectral Micro-Satellite,” University of Bristol Master’s thesis, 2012.

[5] M. Leomanni, A. Garulli, A. Giannitrapani and F. Scortecci, "Propulsion options for very low Earth orbit microsatellites", Acta Astronautica, vol. 133, pp. 444-454, 2017.

[6] GOCE Flight Control Team (HSO-OEG), “GOCE End-of-Mission Operations Report”, ESA, 2014.

[7] K. Fujita and A. Noda, “Aerodynamics of Satellites on a Super Low Earth Orbit”, in AIP Conference Proceedings, Kyoto, 2008.

[8] J. Walsh and L. Berthoud, "Is it possible to integrate Electric Propulsion thrusters on Very-Low Earth Orbit Microsatellites?" Space Propulsion, Rome, 2016.

[9] J. Walsh and L. Berthoud, "Reducing spacecraft drag in Very Low Earth Orbit through shape optimisation", 7th European Conference for Aeronautics and Aerospace Sciences (EUCASS), Milan, 2017.

[10] L. Sentman, "Free molecule flow theory and its application to the determination of aerodynamic forces" Tech. rep. 1961.

[11] D. Vallado and D. Finkleman, “A Critical Assessment of Satellite Drag and Atmospheric Density Modeling”, Acta Astronautica, vol. 95, no. 1, pp. 141 -165, 2014.

[12] L. Brieda, J. Pierru, R. Kafafy and J. Wang, “Development of the DRACO Code for Modeling Electric Propulsion Plume Interactions,” 40th AIAA/ASME/SAE/ASEE Joint Propulsion Conference and Exhibit, AIAA Paper 2004-3633, July 2004.

[13] K. Stephani, I. Boyd, R. Balthazor, M. McHarg, A. Mueller and R. Adams, “Analysis and Observation of Spacecraft Plume/Ionosphere Interactions During Maneuvers of the Space Shuttle,” Journal of Geophysical Research: Space Physics, vol. 119, pp. 7636–7648, 2014. [14] J. Wang, Y. Cao, R. Kafafy, J. Pierru and V. Decyk, “Simulations of Ion Thruster Plume—Spacecraft Interactions on Parallel Supercomputer,” IEEE Transactions on Plasma Science, vol. 34, no. 5, pp. 2148–2158 Oct. 2006.

[15] O. Tumuklu and D. Levin, "Particle Simulations of the Effects of Atomic Oxygen on Ion Thruster Plumes," Journal of Spacecraft and Rockets, vol. 55, no. 5, 2018.

[16] S. Andrews and L. Berthoud, "Characterisation of the Aerodynamic Interactions of Ion Thruster Plume Plasmas in Very Low Earth Orbit," Acta Astronautica [in press], 2018.

[17] S. Andrews and L. Berthoud, "Modelling and Characterisation of Plasmadynamic Drag on Gridded Ion Engine Propelled Spacecraft in Very Low Earth Orbit", Proceedings of the 69th International Astronautical Congress (IAC) 2018, Bremen, Oct. 2018.

[18] S.Andrews, "Modelling Plasmadynamic Drag of Gridded Ion Engine Propelled Satellites in VLEO," University of Bristol Bachelor's Thesis, 2018.

[19] D. Levandier and Y. Chiu, “A Guided-Ion Beam Study of the Reactions of Xe^+ and Xe^{2+} with NH_3 at Hyperthermal Collision Energies,” Journal of Chemical Physics, vol. 133, no. 15, Oct. 2010.

[20] M. Bastian, A. Dressler and E. Murad, “Guided-Ion Beam Measurements of the $O^+(4S) + Xe$ Charge-Transfer Reaction,” Journal of Chemical Physics, vol. 103, no. 1, pp. 144–149, 1995.

[21] B. Prince and J. Bemish, “Space Vehicle Chemical Interactions and Technologies,” Report: RV-PS- TR-2015-0110, U.S. Air Force Research Lab., Wright-Patterson AFB, OH, May 2015.

[22] B. Korkut and D. Levin, “Three-Dimensional Simulations of Backflows from Ion Thruster Plumes Using Unstructured Grid Refinement,” Journal of Propulsion and Power, vol. 33, no. 1, pp. 264–275., Jan. 2017.

[23] D. Rapp and W. Francis, “Charge Exchange Between Gaseous Ions and Atoms,” Journal of Chemical Physics, vol. 37, no. 11, pp. 2631–2645, Dec. 1962.

[24] H. Matsumoto and K. Koura, “Comparison of Velocity Distribution Functions in an Argon Shock Wave Between Experiments and Monte Carlo Calculations for Lennard–Jones Potential,” Physics of Fluids A: Fluid Dynamics, vol. 3, no. 12, pp. 3038–3045, Dec. 1991.

[25] G. Bird, Molecular Gas Dynamics and the Direct Simulation of Gas Flows, Clarendon Press, Oxford, England, U.K., 1994.

[26] C. Birdsall, “Particle-in-Cell Charged-Particle Simulations, Plus Monte Carlo Collisions with Neutral Atoms, PIC-MCC,” IEEE Transactions on Plasma Science, vol. 19, no. 2,pp. 65–85, 1991.

[27] G. Bird, The DSMC Method, CreateSpace Independant Publishing Platform, 2013.

[28] I. Boyd, "Conservative species weighting scheme for the direct simulation Monte Carlo method," J. Thermophys. Heat Tr., vol. 10, no. 4, pp. 579–585, 1996.

[29] C. Birdsall, and A. Langdon, Plasma Physics Via Computer Simulation, Taylor and Francis, New York, 2004.

[30] D. VanGilder, “Numerical Simulations of the Plumes of Electric Propulsion Thrusters,” P.D. Thesis, Cornell Univ., Ithaca, NY, 2000.

[31] A. Passaro, L. Biagioni, and A. Vicini, "Plasma Thruster Plume Simulation: Effect of the Plasma Quasi Neutrality Hypothesis," 34th AIAA Plasmadynamics and Lasers Conference, Orlando, 2003.

[32] M. Santi, S. Cheng, “Further Development and Preliminary Results of the AQUILA Hall Thruster Plume Model,” 39th Joint Propulsion Conference, Huntsville, Alabama, 2003.

[33] L. Brieda and M. Keidar, "Multiscale Modelling of Hall Thrusters," 33rd International Electric Propulsion Conference, 2011.

[34] L. Brieda, and M. Keidar, “Development of the Starfish Plasma Simulation Code and Update on Multiscale Modeling of Hall Thrusters”, 48th AIAA Joint Propulsion Conference, Atlanta, GA, 2012.

[35] F. Crary and D. Young, "Charge Exchnage Ions Produced by an Ion Propulsion System," 39th AIAA Aerospace Sciences Meeting and Exhibit, Jan. 2001.

[36] R. Dressler, M. Bastian, D. Levandier, and E. Murad, "Empirical model of the state-to-state dynamics in near-resonant hyperthermal $X^+ + H_2O$ charge-transfer reactions," Int. J. Mass Spectrom. Ion Processes, vol. 159, pp. 245–256, 1996.

[37] S. Miller, S. Pullins, D. Levandier, Y. Chiu and R. Dressler, “Xenon Charge Exchange Cross Sections for Electrostatic Thruster Models,” Journal of Applied Physics, vol. 91, no. 3, pp. 984–991, 2002.

[38] G. Lindsay and R. Stebbings, “Charge Transfer Cross Sections for Energetic Neutral Atom Data Analysis,” Journal of Geophysical Research, vol. 110, no. 12, 2005.

[39] N. Sack, M. Akbulut and T> Madey, “Transmission of Low-Energy O^+ Ions Through Ultrathin Films of Ar, Kr, and Xe,” Physical Review B, vol. 51, no. 7, 1995.

[40] J. Picone, A. Hedin, D. Drob and C. Aikin, "NRLMSISE-00 empirical model of the atmosphere: Statistical ...," Journal of Geophysical Research: Space Physics, vol. 107, no. A12, p. 1468, 1991.

[41] M. Crofton, "Evaluation of the T5 (UK-10) Ion Thruster: Summary of Principal Results," in IEPC-95-91, 1995.

[42] J. Pollard, "Plume angular, energy, and mass spectral measurements with the T5 ion engine," 31st Joint Propulsion Conference and Exhibit, Joint Propulsion Conferences, AIAA95-2920, San Diego, 1995.

[43] N. Wallace, P. Jameson, C. Saunders, M. Fehringer and C. Edwards, "The GOCE Ion Propulsion Assembly Lessons Learnt from the First 22 Months of Flight Operations," International Electric Propulsion Conference, IEPC-2011-327, Wiesbaden, 2011.

[44] D. Mundy and D. Fearn, "Throttling the T5 ion engine over a wide thrust range," 33rd Joint Propulsion Conference, Seattle, USA, 2012.

[45] P. Randall, R. Lewis and S. Clark, "QinetiQ T5 based Electric Propulsion System and Architectural Options for Future Applications," 35th International Electric Propulsion Conference, Atlanta, USA, 2017.